AGU PUBLICATIONS

Tectonics

RESEARCH ARTICLE
10.1002/2017TC004782

Key Points:
- Growth models predict hard linkage of underlapping extensional step over segments
- Forecasts reveal sensitivity of fault propagation to rock heterogeneities
- Fault tip stress field and anisotropy compete to control fault growth

Supporting Information:
- Supporting Information S1

Correspondence to:
J. McBeck,
j.a.mcbeck@geo.uio.no

Citation:
McBeck, J., Cooke, M., & Madden, E. (2017). Work optimization predicts the evolution of extensional step overs within anisotropic host rock: Implications for the San Pablo Bay, CA. *Tectonics*, *36*. https://doi.org/10.1002/2017TC004782

Received 24 AUG 2017
Accepted 19 OCT 2017
Accepted article online 4 NOV 2017

Work Optimization Predicts the Evolution of Extensional Step Overs Within Anisotropic Host Rock: Implications for the San Pablo Bay, CA

Jessica McBeck[1,2], Michele Cooke[1], and Elizabeth Madden[1,3]

[1]Department of Geosciences, University of Massachusetts Amherst, Amherst, MA, USA, [2]Now at Physics of Geologic Processes, Department of Geosciences, University of Oslo, Oslo, Norway, [3]Department of Earth and Environmental Sciences, Department of Geophysics, Ludwig-Maximilians-Universität München, Munich, Germany

Abstract Recent geophysical imaging indicates that the Hayward Fault hard links to the Rodgers Creek Fault at 5 m depth within the San Pablo Bay, CA, suggesting that earthquakes may be able to rupture continuously through the fault network. To investigate fault propagation, interaction, and linkage in segmented fault networks, including those within the San Pablo Bay, we simulate the development of two idealized, underlapping faults within an extensional step over at seismogenic depths using work optimization. We test the sensitivity of fault growth to strength anisotropy, material heterogeneities, and initial fault geometry. The optimal faults propagate toward each other until linking with the other fault at its tip and form a single hard-linked transverse fault. These faults propagate with relatively high propagation power or rate of efficiency gain. Less efficient faults form wider basins and develop with reduced propagation power. Models with initial fault geometries that more closely match the shallowly imaged Hayward and Rodgers Creek faults suggest that the faults link at seismogenic depths if a mapped segment of the Rodgers Creek that extends into the San Pablo Bay is currently inactive. Predictions of average slip rate, slip per earthquake, and earthquake magnitude from these models closely match paleoseismic estimates. The hard linkage of the Hayward and Rodgers Creek faults imaged in the near-surface, and predicted by these models, increases local seismic hazard by increasing the upper limit of throughgoing earthquakes to *M* 7.6.

1. Introduction

In the San Francisco Bay area in CA, USA, the Rodgers Creek-Hayward Fault network is predicted to have the highest likelihood of producing a $\geq M$ 6.7 earthquake in the next 30 years (32%, Field et al., 2015). The surficial traces of the southern end of the dextral Rodgers Creek Fault and northern end of the dextral Hayward Fault are separated by an extensional step over within the San Pablo Bay, to the northeast of San Francisco (Figure 1). Interpretations of seismic reflection and refraction data indicate that within the upper 1–2 km the Rodgers Creek and Hayward faults are laterally separated by ~4 km (e.g., Parsons et al., 2003). Recent ultrahigh-resolution seismic reflection cross sections attained with a chirp subbottom profiler suggest that a throughgoing transfer fault links the tip of the Hayward Fault with the Rodgers Creek Fault within 2–5 m of the surface (Figure 1) (Watt et al., 2016). This geophysical imaging informs the present-day fault geometry within the shallow subsurface (e.g., Watt et al., 2016). To assess seismic hazard in the San Francisco Bay region, we must confirm if the faults are linked at seismogenic depths. Paleoseismic evidence and numerical models show that seismic rupture is arrested when the perpendicular separation between segmented strike-slip faults is $>$5 km and that rupture is more likely to propagate across step overs with smaller separations (e.g., Harris & Day, 1999; Lettis et al., 2002; Wesnousky, 2008). Here we model the potential evolution of the Hayward-Rodgers Creek Fault network to evaluate the possibility of their linkage at seismogenic depths and assess the likelihood of ruptures to continue or arrest.

In order to gain a first-order understanding of fault growth within extensional step overs, we first simulate the propagation and interaction of two idealized underlapping, planar faults. We model the propagation of these faults in the directions that optimize work using the numerical modeling tool Growth by Optimization of Work (GROW) (Madden, et al., 2017; McBeck et al., 2016). Following this investigation, we model interaction between faults that more closely match the geometry of the southern strand of the Rodgers Creek Fault and the northern strand of the Hayward Fault. Metamorphosed basement rock, such as the serpentinite in the Franciscan Complex within the San Pablo Bay region (e.g., Wakabayashi, 1992), can exert a strong control

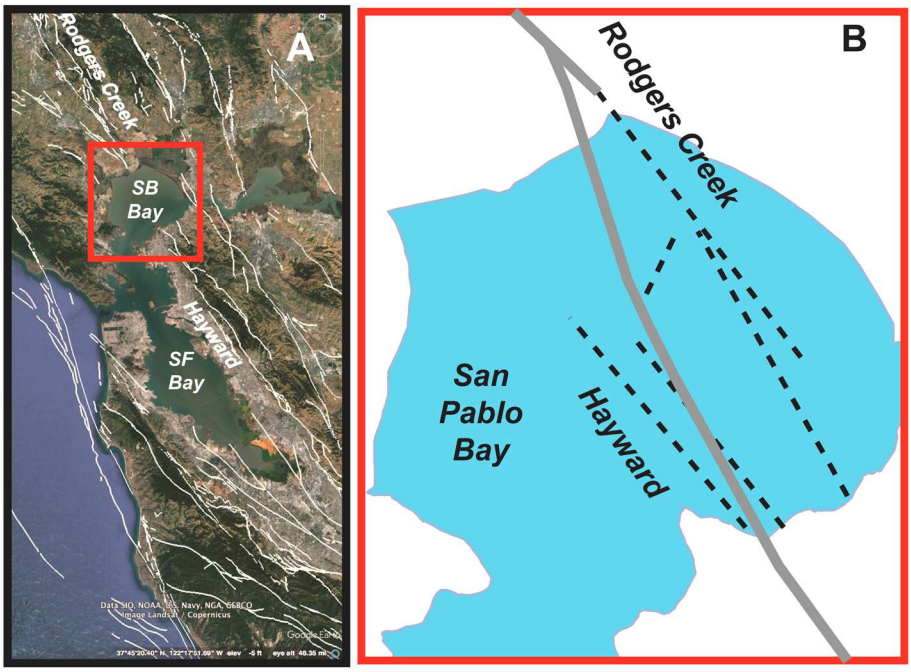

Figure 1. (a) Context map with Google Earth image (map data: Google, SIO, NOAA, U.S. Navy, NGA, GEBCO, and Image Landsat/Copernicus) and quaternary faults from USGS fault and fold database (white) (US Geological Survey and California Geological Survey). The red box indicates study area shown. (b) Fault geometry of step over from previous interpretations in black dashed lines (Parsons et al., 2003) and more recent interpretations in solid gray lines (Watt et al., 2016).

on fault propagation path. Consequently, we investigate the sensitivity of fault growth to pervasive host rock strength anisotropy for both suites of models.

2. Background

In this study, we investigate the interaction and linkage of planar underlapping faults, as well as the propagation of the Hayward Fault toward the Rodgers Creek Fault. We review past work on the evolution of idealized, on the planar segmented fault networks, and on the regional tectonics of the San Pablo Bay.

2.1. Extensional Step Over Evolution in Anisotropic Host Rock

Understanding the evolution of propagating faults is key to constraining seismogenic hazard and identifying potential fluid flow paths, including groundwater and hydrocarbons. Field observations, scaled physical analog experiments, and numerical and analytical techniques have provided insight into the mechanisms that control fault evolution (e.g., Cooke et al., 2016; Ferrill et al., 2007). Interpretations of field observations provide critical constraints on the geometry of strike-slip faults separated by extensional step overs in crustal environments (e.g., Mann et al., 1983). Field observations suggest that extensional step overs initially develop as narrow basins bounded by faults that directly connect the strike-slip fault segments (Figure S1 in the supporting information) (e.g., Mann et al., 1983).

Segmented fault networks develop in mechanically anisotropic crust, where fault segments form along weak interfaces (e.g., Morley, 2007). Interfaces that provide strength anisotropy include preexisting fracture sets, sedimentary layering, schistocity, and other foliation (e.g., Chester & Fletcher, 1997). Field observations suggest that preexisting basement fabrics (e.g., Morley et al., 2004), preexisting faults (e.g., Zampieri et al., 2003), and stratigraphy within limestone and shale sequences (e.g., Ferrill et al., 2007) provide mechanical anisotropy that influences fault development. For example, zones of weakness in prerift sediments or crystalline rocks have been observed to exert a first-order control on continental rift development (e.g., Cunningham & Mann, 2007; Daly et al. 1989; Dixon et al., 1987; McConnell, 1972; Morley et al., 2004; Morley, 2007; Smith & Mosley, 1993).

Quantitative monitoring of scaled physical experiments enables direct observation of the kinematic evolution of step over fault systems (e.g., Cooke et al., 2013; Dooley & Schreurs, 2012; Hatem et al., 2015; McClay & Dooley, 1995). Scaled physical experiments of extensional basin evolution indicate that during the initial stages of basin development, obliquely slipping normal faults propagate from the main fault segments and form a narrow graben connecting the segments (e.g., Dooley et al., 1999; Dooley & Schreurs, 2012; Rahe et al., 1998). The initial geometry of the parallel fault segments controls the graben geometry: underlapping fault segments typically form elongate, rhomboidal grabens, while overlapping fault segments develop box-like, rhomboidal grabens (e.g., Dooley & McClay, 1997; McClay & Dooley, 1995).

Scaled physical experiments can also capture the influence of preexisting faults on fault development (e.g., Bellahsen & Daniel, 2005; Bonini et al., 1997; Del Ventisette et al., 2006; Dubois et al., 2002; Faccenna et al., 1995; Henza et al., 2010; Sassi et al., 1993). Physical experiments reveal that both preexisting faults and the orientation of principal stresses control the subsequent development of both compressional and extensional structures (Del Ventisette et al., 2006; Henza et al., 2010). In addition, triaxial compression tests of layered rocks show that the geometry of newly propagated faults changes with the orientation of the layering relative to the applied principal stresses (e.g., Peacock & Sanderson, 1992).

Numerical simulations allow analysis of the complete stress and strain field within segmented fault systems (e.g., Bürgmann et al., 1994; Cowie et al., 2000; Crider & Pollard, 1998; Kattenhorn & Pollard, 2001; Li et al., 2009; Willemse, 1997), and so provide additional constraints on the factors that control fault development within anisotropic systems (e.g., Duan & Kwok, 2016; Duan et al., 2016; Gudmundsson et al., 2010; Lisjak et al., 2014; Misra et al., 2015; Tong & Yin, 2011) beyond those gleaned from field observations and physical experiments. For example, DEM modeling of borehole breakouts indicates that material anisotropy exhibits a stronger influence on fracture development near the borehole when the borehole is drilled perpendicular to bedding in simulated shale than when it is drilled parallel to bedding (Duan & Kwok, 2016). In addition, an analytical solution for the distribution of stress produced by sliding on a wavy frictionless fault within anisotropic material (Chester & Fletcher, 1997) indicates that as the magnitude of anisotropy increases, the patterns of shear failure within contractional and extensional step overs become increasingly similar because the anisotropy controls failure to a greater extent than the variation in fault geometry.

2.2. Regional Tectonics of the San Pablo Bay Area

The Hayward and Rodgers Creek faults are part of a complex fault network that lies to the east of the San Andreas Fault, within the San Francisco Bay area of northern California, USA. The bedrock of this region is primarily the Franciscan Complex, which includes variably deformed and metamorphosed rock from sediments accreted along the western North American plate margin due to subduction of the Farallon slab (e.g., Wakabayashi, 1992). After subduction ceased, major right-lateral strike-slip faults, including the San Andreas, developed within the Franciscan to accommodate horizontal convergence across the Pacific plate and western North American plate boundary (e.g., Wakabayashi, 1992). The Franciscan includes detrital sedimentary rocks (mostly sandstones), serpentinite, basaltic volcanic rocks, chert, and minor limestone (Bailey et al., 1964; Blake et al., 1984; Coleman, 2000; Wakabayashi, 2004, 2012). Near the San Pablo Bay, the Franciscan Complex consists of a stack of coherent nappes separated by low-angle mélange zones that were folded about NW-SE subhorizontal fold axes (Blake et al., 1984; Wakabayashi, 1992). The Franciscan Complex is thus anisotropic from the mm to km scale, as it includes aligned minerals and folded mélange zones (e.g., Bailey et al., 1964; Wakabayashi, 1992). The ~NW trend of the accreted nappes suggests that the dominant strength anisotropy arising from aligned minerals and weak interfaces likely parallels or subparallels the strikes of the Hayward and Rodgers Creek faults (e.g., Wakabayashi, 1992).

Recent interpretations of geophysical imaging within the upper 5 m of sediments in the San Pablo Bay (Watt et al., 2016) refine the previously interpreted fault evolution of McLaughlin et al. (2012). These recent interpretations suggest that at ~8 Ma, changes in plate motion lead to transpression and fault reorganization within the San Pablo Bay (Watt et al., 2016). After this reorganization, a locally transtensional basin developed between the southern segment of the Rodgers Creek and northern segment of the Hayward. After ~7 Ma, the Hayward Fault propagated north toward and linked with the Rodgers Creek Fault (Watt et al., 2016).

3. Methods

To model fault evolution, we use the software GROW (GRowth by Optimization of Work) (Madden et al., 2017; McBeck et al., 2016), which simulates fault growth using work optimization within materially heterogeneous host rock with strength anisotropy. We detail the loading conditions, initial fault geometry, and material and fault properties of models presented here.

3.1. Simulating Fault Development With GROW

GROW simulates fracture propagation within 2-D plane strain by adding elements to growing fracture tips in the radial orientation that optimizes the resulting change in external work, W_{ext}, divided by the added new fracture area, $\Delta W_{ext}/\Delta A$ (McBeck et al., 2016). In the 2-D systems considered here, W_{ext} may be calculated by integrating over the loading path, L, the sum of the products of shear traction and displacement, τ and u_s, and normal traction and displacement, σ_n and u_n, integrated over the system boundaries, B:

$$W_{ext} = \int_L \iint_B (\tau u_s + u_n \sigma_n) dB dL \quad (1)$$

To find the boundary tractions and displacements required to calculate W_{ext}, GROW repeatedly calls the boundary element method program Fric2D (Cooke & Pollard, 1997). In Fric2D, boundaries and fractures are discretized into linear segments that may open or slip, but not interpenetrate, in response to tractions or displacements applied to the boundaries or perturbations from other fractures. Fric2D models simulate 2-D plane strain, in which the model is considered to extend 1 m in the third dimension. Thus, the fracture area is the fracture length multiplied by 1 m.

In GROW, fractures stop propagating when fractures link with other fractures or the model boundaries, or when none of the radial elements added to the tip of a fracture fail in tension or shear (McBeck et al., 2016). An element fails in tension when the normal traction (tension positive) exceeds or equals the tensile strength of the intact rock at the fault tip. A potential growth element fails in shear following the Coulomb criterion, when the magnitude of the shear traction exceeds or equals the difference between the inherent shear strength and the product of the internal coefficient of friction and normal traction across the potential element.

3.2. GROW Fault Development in Anisotropic Systems

In order to predict the evolution of fracture networks in complex crustal materials, GROW parameterizes fault propagation through material with anisotropic strength. This development provides a new functionality since McBeck et al. (2016) and Madden et al. (2017). The strength anisotropy may be applied with one or more of the host rock material properties used in GROW, such as the inherent shear strength or internal friction coefficient. Anisotropy is set relative to a two-dimensional global coordinate system that is measured clockwise from the left horizontal plane. When a fault propagates, the orientation of the growth element relative to this global coordinate system determines the value of the anisotropic property assigned to the element. This value is identified in a look-up table that contains all specified global orientations and associated property values.

GROW cannot yet simulate fault propagation through material with elastic anisotropy (e.g., Brownlee et al., 2017). Pronounced anisotropic elastic properties could alter the local stress field and induce faults to deviate from the work optimal path predicted in elastically isotropic systems. Because crustal rocks contain abundant planes of weakness, we expect that the impact of strength anisotropy on fault propagation will exceed that of elastic anisotropy of the host rock between the interfaces, and so only consider anisotropic strength in this study.

Strength anisotropy may be present in host rocks with preexisting stratigraphic layering, fracture sets, or metamorphic fabric (e.g., Chester & Fletcher, 1997). This function of GROW is particularly beneficial for simulating fault propagation within the San Pablo Bay, because the NW-SE trend of the metamorphosed Franciscan Complex provides strength anisotropy at a wide range of scales within the San Francisco Bay region (e.g., Wakabayashi, 1992) and because wall rock strength appears to influence the distribution of seismic activity on the Hayward Fault (Graymer et al., 2005).

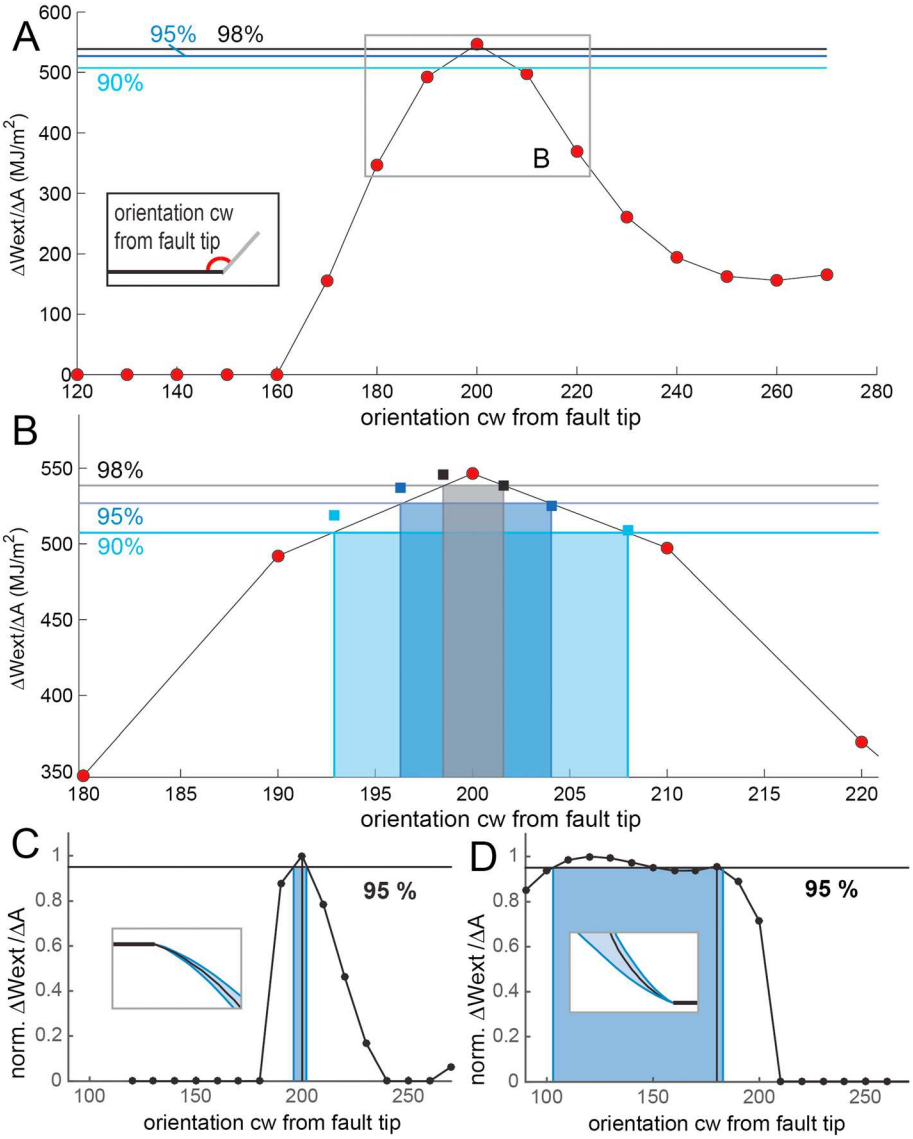

Figure 2. Construction of propagation forecasts of fault growth. (a) Distribution of $\Delta W_{ext}/\Delta A$ calculated in initial search for efficient propagation path orientation (red dots). The horizontal lines show the percentage, p, multiplied by the maximum $\Delta W_{ext}/\Delta A$ at the increment of growth, $p\frac{\Delta W_{ext}}{\Delta A}$. (b) Close up of box in Figure 2a. The blue rectangles indicate range of potential fault element orientations that produce $\Delta W_{ext}/\Delta A$ greater or equal to $p\frac{\Delta W_{ext}}{\Delta A}$. The squares show $\Delta W_{ext}/\Delta A$ calculated for fracture geometries that include an element at each interpolated angle. Hypothetical distributions of $\Delta W_{ext}/\Delta A$ with (c) narrow peak and (d) broad distribution.

3.3. GROW Propagation Forecasts

GROW is able to capture the epistemic uncertainties introduced by fault propagation and interaction within heterogeneous materials by building propagation forecasts of fault growth (Madden et al., 2017). These propagation forecasts outline the range of possible fracture paths due to the presence of heterogeneities that may induce growing faults to deviate from the optimal propagation path. At each increment of growth, GROW finds $\Delta W_{ext}/\Delta A$ produced by the addition of each potential element radial to the growing fracture tip (Figure 2a). GROW then identifies the range of element orientations within a certain percentage of the maximum $\Delta W_{ext}/\Delta A$, which is the optimal growth direction. Next, GROW adds an element to the growing fault at one of limits of this range, either the largest or smallest element orientation, and continues fault growth from this new element tip. To develop the propagation envelope, two scenarios are modeled, which reflect the two limits of the investigated $\Delta W_{ext}/\Delta A$ range.

When the differences between $\Delta W_{ext}/\Delta A$ produced by similarly oriented elements are small, the distribution of $\Delta W_{ext}/\Delta A$ is broad and produces a wide propagation forecast envelope (Figures 2c and 2d). A wide

envelope indicates that local heterogeneities can promote propagation away from the optimal path. If many propagation orientations are similarly efficient in an isotropic material, a fault may propagate into a weaker area (with low tensile strength due to lesser lithification, for example) rather than into a neighboring area. Conversely, when the differences between $\Delta W_{ext}/\Delta A$ produced by elements are large, the distribution of $\Delta W_{ext}/\Delta A$ has a well-defined peak, and the propagation forecast is narrow, closely enveloping the optimal growth path (Figures 2c and 2d). In this case, fault propagation is relatively insensitive to local heterogeneities, and even if a host rock contains neighboring areas with somewhat higher and lower tensile strengths, the stress field and fault geometry will continue to favor fault propagation along the most efficient orientation predicted in the isotropic system. We present the GROW propagation forecasts with the percentage of the maximum $\Delta W_{ext}/\Delta A$ equal to 90% and 95%.

3.4. Loading Conditions

To simulate the development of the Rodgers Creek and Hayward faults, we superpose the model boundary displacements due to lithostatic confining stress and the displacements due to tectonic motion that accumulate over several thousand years. Relocated earthquake hypocenters (Waldhauser & Schaff, 2008; version v201112.1) indicate that the seismogenic zone beneath San Pablo Bay extends from ~7 to 12 km. We calculate the effective lithostatic stress at a depth of 12 km with the density of typical mafic rock (2,700 kg/m^3) and density of fluid (1,000 kg/m^3). The fault parallel and perpendicular strains due to lithostatic stress are derived using Hooke's 2-D plane strain relationships. To calculate the tectonic strains, we find the total strain expected to accumulate over several thousand years from the components of the regional strain rate tensor as constrained by geodesy (Pollitz & Nyst, 2005). The best fitting uniform horizontal strain field for the San Francisco Bay region has principal strain rates of $\dot{\varepsilon}_{11}$ = 164.7 ± 7.2 nanostrain/yr and $\dot{\varepsilon}_{22}$ = −157.9 ± 6.9 nanostrain/yr oriented N74.0°W and N16.0°E, respectively, with contraction negative (Pollitz & Nyst, 2005). A coordinate transformation of the principal strain rate tensor provides the components of the strain rate tensor parallel and perpendicular to the fault strikes due to tectonic motion, $\dot{\varepsilon}_{ij}$. The total strain that accumulates over t years due to long-term tectonic motion is then $\dot{\varepsilon}_{ij}t$. The total strain parallel and perpendicular to the faults due to tectonic motion and lithostatic stress are summed and converted to displacements using the initial width, w, and height, h, of the model domain. The normal displacements applied to the top model boundary are calculated from the change in model height due to the total normal strain perpendicular to the faults, $h\varepsilon_{yy}$. The normal displacements applied to the right boundary are calculated from the change in model width due to the normal strain parallel to the faults, $w\varepsilon_{xx}$. We apply the displacements due to ε_{xy} on the model sides with a stepwise distribution across the faults.

We progressively increase the applied displacements until either the faults link or the total loading corresponds to 5,000 years of deformation. This loading is suitable for simulating the steady state fault interaction here because it encompasses several earthquake cycles, which have recurrence rates of 230 and 710 years (e.g., Hayward Fault Paleoearthquake Group, 1999; Schwartz et al., 1992). Because low levels of loading do not produce enough stress to induce fault propagation, the progressive loading begins with applied displacements corresponding to 2,500 years of deformation, and then we increase the loading in steps of 500 years. Because the faults within our models creep, we do not investigate slip events and instead each modeling step captures the steady state deformation that would accumulate under the applied loading. It should be noted that the dynamic effects of rupture propagation are not considered in this study and could impact fault propagation.

3.5. Anisotropy of Internal Friction

Although laboratory strength experiments have been exacted on intact wafers of anisotropic rocks with foliation planes of phyllosilicates (e.g., Collettini et al., 2009), constraints on the anisotropy of internal friction within serpentinite have remained elusive. The direction of planes of weakness, which is captured by the anisotropy direction in these models, is likely controlled by the orientation of foliation planes of weak minerals (e.g., Collettini et al., 2009; Escartin et al., 1997; Moore & Lockner, 2004). Within foliated metamorphic host rock that contains serpentinite, such as the Franciscan Complex, preferential mineral alignment tends to reduce the internal friction along one or a few dominant orientations (e.g., Collettini et al., 2009), and likely at orientations within a few degrees of the preferred orientation. Accordingly, we define an internal friction

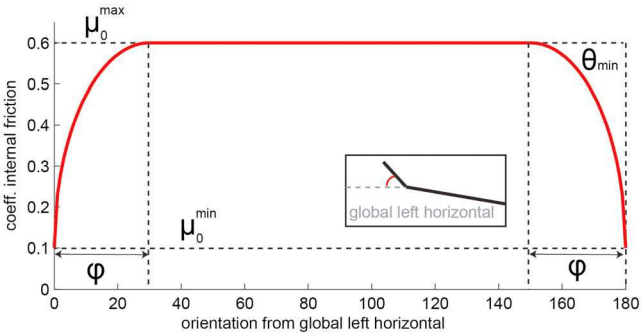

Figure 3. An anisotropic distribution of internal friction coefficient, μ_0, used in this study. The orientation at which μ_0 is minimized, θ_{min} (180°); the magnitude of the minimum friction coefficient, μ_0^{min} (0.1); the magnitude of the maximum friction coefficient, μ_0^{max} (0.6); and the degrees from θ_{min} at which the friction is maximized, φ (30°), control the friction distribution. Orientation is measured from the global left horizontal plane.

distribution that incorporates diminishing frictional strength near the dominant preferred orientation, rather than a stepwise function with only two maximum and minimum values of internal friction, for example.

Specifically, we parameterize host rock anisotropy by varying the internal friction coefficient, μ_0. The distribution of μ_0 is controlled by the orientation at which the internal friction is minimized, θ_{min}; the magnitude of the minimum internal friction coefficient, μ_0^{min}; the magnitude of the maximum internal friction coefficient, μ_0^{max}; and the degrees from θ_{min} at which the internal friction reaches maximum, φ. The global orientation that determines μ_0, θ, is measured clockwise from the left horizontal plane (Figure 3). In this analysis, we set the distribution of internal friction as an ellipse with horizontal radius of φ and vertical radius of $\mu_0^{max} - \mu_0^{min}$ (Figure 3):

$$\frac{(\theta - (\theta_{min} - \varphi))^2}{\varphi^2} + \frac{(\mu_0 - \mu_0^{min})^2}{(\mu_0^{max} - \mu_0^{min})^2} = 1 \quad (2)$$

Varying θ_{min} indicates how the direction of pervasive strength anisotropy influences fault development, while varying μ_0^{min} reveals the influence of the magnitude of the anisotropy on fault development.

Field observations suggest that the dominant anisotropy direction within the San Pablo Bay parallels or subparallels the strike of the fault segments (e.g., Wakabayashi, 1992). Accordingly, we vary the orientation of μ_0^{min} from θ_{min} = 160–200°, as the orientation of the parallel segments of the faults is at 180°. We vary μ_0^{min} from 0.1 to 0.4 and keep μ_0^{max} constant at 0.6, consistent with laboratory strength measurements on rocks containing weak mineral phases (e.g., Holdsworth et al., 2011; Lockner et al., 2011; Morrow & Lockner, 2001).

3.6. Initial Fault Geometry

We simulate fault growth in two suites of models that contain three unique initial fault geometries (Figure S2). First, we study fault interaction within a simplified fault geometry, in which the perpendicular separation distance between the underlapping, parallel, planar faults matches the approximate distance between the subparallel strands of the Rodgers Creek and Hayward faults from Watt et al. (2016). In the second set of models, the initial fault geometries follow those inferred from two sets of geophysical observations, including earlier work (Parsons et al., 2003), and more recent imaging (Watt et al., 2016). Earlier geophysical data indicate that the Rodgers Creek Fault extends far into the San Pablo Bay (Parsons et al., 2003), forming an overlapping step over with the Hayward Fault. However, Watt et al. (2016) do not find evidence for activity along this fault in the upper 2–5 m and map an underlapping step over within the bay. In order to shed insight on the active geometry of the Rodgers Creek Fault, we develop models with two initial Rodgers Creek Fault geometries that span this epistemic uncertainty (Figure S2) and model propagation of the Hayward Fault.

In these 2-D plane strain models, the faults are considered to have vertical dips. Dipping faults could accommodate greater extension across this extensional step and subsequently greater local subsidence than the modeled fault segments. Because the strike-slip rates along the underlapping strike-slip fault segments are typically greater than their local dip-slip rates, the along-strike propagation of the faults is predominantly driven by the strike slip along these faults, which is captured in the plane strain models.

3.7. Material and Fault Properties

The prescribed material properties represent mafic, metamorphosed rock similar to the Franciscan Complex (Table 1). The coefficients of internal, static, and dynamic friction are within measurements from laboratory strength experiments (e.g., Byerlee, 1978; Lockner et al., 2011). We use zero inherent shear strength and zero tensile strength, which allows the widest range of potential fault propagation paths. Among these paths, GROW finds the optimal path that produces the largest $\Delta W_{ext}/\Delta A$. Implementing low strength provides an expeditious approach for finding the optimal orientation without having to determine scale-independent representative crustal strength values. Correspondingly, we do not aim to simulate the number of years required to propagate the faults, but rather to predict the long-term evolution of fault geometry in the

Table 1
Representative Intact Rock and Fault Properties Used in Models (e.g., Byerlee, 1978; Lockner et al., 2011; Morrow & Lockner, 2001)

Property	Value
Poisson's ratio	0.25
Young's modulus	60 GPa
Density	2700 kg/m^3
Tensile strength	0 MPa
Inherent shear strength	0 MPa
Internal friction coefficient	0.6
Cohesion	0 MPa
Static and dynamic friction coefficient	0.1
Slip-weakening distance	2 m

step over. Increasing the tensile or shear strength changes the magnitude of the loading required for fault propagation, but the orientation of the most efficient element does not change.

To determine the appropriate length of the fault and boundary elements, we perform a discretization analysis that is described in full in the supporting information. Systematic variation of element length reveals that a length of 250 m provides a robust compromise between the model solution ($\Delta W_{ext}/\Delta A$) and model run time (Figure S3).

4. Predictions of Simplified Fault Development

First, we describe the predicted fault propagation paths and evolutions of efficiency with fault growth in the planar, underlapping fault configuration models. We examine the resulting propagation paths in host rocks with both isotropic and anisotropic strengths. Propagation envelopes that consider heterogeneous material are investigated for the isotropic models.

4.1. Propagation Forecasts of Simplified Faults

For the simplified fault models, the most efficient, or optimal, propagation path of each fault gently curves toward the other fault until linking with the other fault (Figure 4a). The width of the basin between the two faults increases as the sensitivity of fault propagation to heterogeneities is increased, that is, as the propagation forecast decreases from 95% to 90% of optimal change in work (Figure 4a). The geometry of the 90% propagation forecast defines the widest basin. The zone of the 95% propagation forecast is about half as wide as the 90% zone and forms a shape similar to the narrow basins that develop early in extensional step over evolution (e.g., Figure S1) (e.g., Mann et al., 1983).

The distribution of $\Delta W_{ext}/\Delta A$ in the first increment of growth provides insight into these resulting propagation forecasts (Figure 4b). In the first fault growth increment, for the elements added to the upper left fault tip, the outside limit of the 95% propagation forecast is 4° from the optimal orientation, whereas the inside limit of the 95% propagation forecast is 2° from the optimal orientation. This asymmetry to the $\Delta W_{ext}/\Delta A$ distribution produces an asymmetric propagation forecast that has a larger area toward the outside of the step over, so that the outside limit of the propagation forecast is farther from the optimal path than the inside limit. Over the first few growth increments, the inside limit of the 95% propagation forecast closely parallels the optimal path and remains within 0.5 km of it (inner red line on Figure 4a). The asymmetry to these limits indicates that small heterogeneities in the host rock are more likely to cause faults to propagate outside the optimal propagation path.

The stress fields surrounding the underlapping fault tips produce the asymmetric distribution of $\Delta W_{ext}/\Delta A$. Elements added at orientations $<180°$ to the growing fault tip do not fail in shear, and so $\Delta W_{ext}/\Delta A = 0$ for these elements (Figure 4b). These elements do not fail because the fault-parallel normal stresses are more compressional outside of the step over, and so inhibit shear failure at these angles.

The evolution of $\Delta W_{ext}/\Delta A$ over sequential increments of fault growth reveals how fault interaction controls the propensity for growth and rate of efficiency gain (Figure 4c). Power is the rate of change in work. Accordingly, the change in $\Delta W_{ext}/\Delta A$ over sequential increments of fracture growth is the propagation power of the fault system (McBeck et al., 2016). After the first increments of growth, the optimal growth path gains efficiency at a faster rate than growth along the outside limits of the 95% and 90% propagation forecasts (Figure 4c), producing higher propagation power. The change in propagation power reveals when the faults begin to interact via soft linkage and when they hard link. When the tips of the faults begin to overlap across the step over, soft linkage is marked by an increase in propagation power (Figure 4c, inset 2). The largest gain in efficiency and highest propagation power occur when the faults hard link (Figure 4c, inset 3).

4.2. Simplified Fault Development Within Rock With Strength Anisotropy

Both the magnitude and direction of pervasive host rock strength anisotropy influence fault propagation (Figure 5). In these parameterizations, we characterize the magnitude of anisotropy by varying the

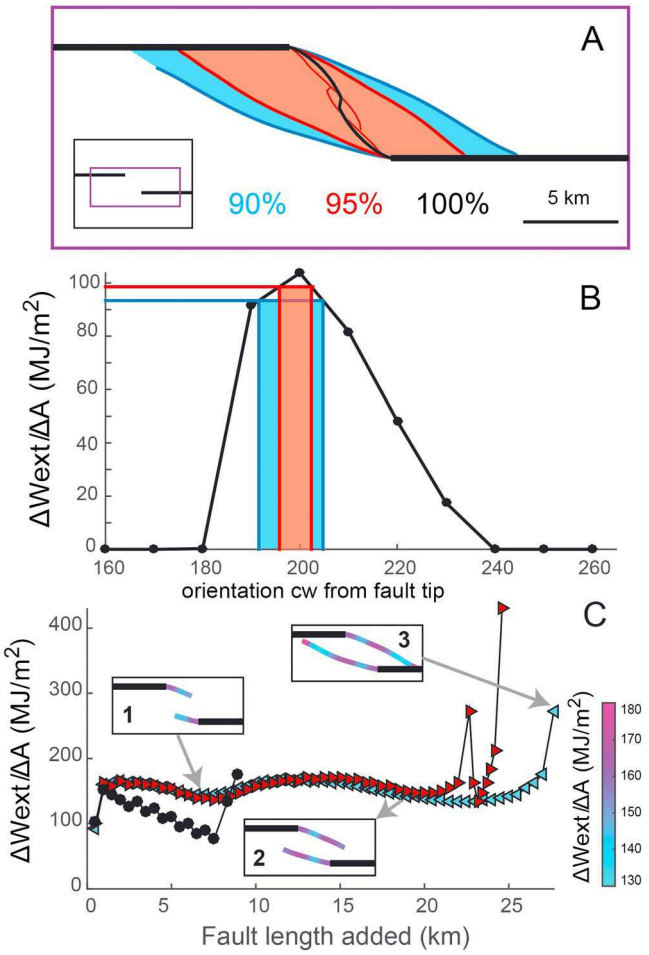

Figure 4. (a) Predicted fault geometries for simplified fault simulations of the optimal propagation path (black), the 95% propagation forecast (red), and the 90% propagation forecast (blue). The red lines inside the shaded region show the inside limits of the 95% propagation forecast. The red and blue lines outside the shaded region show the outside limits of the 95% and 90% forecasts, respectively. The inset figure shows initial fault geometry and model boundaries (black) and figure zoom (purple). (b) Distribution of $\Delta W_{ext}/\Delta A$ produced by addition of one element to the upper left fault tip. Orientation measured clockwise from fault tip. (c) The evolution of $\Delta W_{ext}/\Delta A$ for the optimal growth path (black) and the outside limits of the 95% (red) and 90% (blue) propagation forecasts. The inset figures show fault geometry when (1) faults begin to overlap, (2) after overlap but before hard linkage, and (3) hard linkage. The colors of fault elements in insets are $\Delta W_{ext}/\Delta A$. Propagation power is the slope of the $\Delta W_{ext}/\Delta A$ curve.

minimum internal friction coefficient, μ_0^{min}, and keeping the maximum internal friction coefficient at 0.6 (Figure 5a). We characterize the direction of anisotropy by changing the orientation of the minimum internal friction coefficient, θ_{min}, from 160 to 200° clockwise from the left horizontal plane.

When faults propagate through material with the highest magnitude of anisotropy tested, $\mu_0^{min} = 0.1$ and $\theta_{min} = 160°$, the resulting fault geometry matches that for the isotropic model (Figures 5a–5c). For this system, the distribution of $\Delta W_{ext}/\Delta A$ produced by all potential growth elements in the first increment of growth has two peaks: one at the weakest direction of the material ($\theta_{min} = 160°$) and one at the optimal orientation arising from the fault tip stress field (200°) (Figure 5b). However, $\Delta W_{ext}/\Delta A$ at 160° is less than $\Delta W_{ext}/\Delta A$ at 200°, producing fault propagation at 200° in the first growth increment and indicating that the influence material anisotropy is weaker than the influence of the fault tip stress field. However, when $\theta_{min} = 180°$, the magnitude of $\Delta W_{ext}/\Delta A$ at 180° is sufficient to shift the optimal orientation from 200° to 180°. The increase in ΔW_{ext} produced by the addition of the 180° fault element arises from the lower μ_0^{min} along this element, which allows for more slip and, consequently, lower tractions along the boundaries to accommodate the applied displacements. In this case, the material anisotropy has greater influence on fault propagation direction than the fault tip stress field. When $\theta_{min} = 200°$, the preference for fault growth along this orientation, which is the same as the optimal orientation for the isotropic models, promotes linkage of the faults (Figure 5c).

The magnitude of the anisotropy ($\mu_0^{max} - \mu_0^{min}$) influences the predicted fault geometry when θ_{min} differs from the most efficient orientation of the isotropic system identified in the first increment of growth (Figures 5d–5i). When $\theta_{min} = 180°$, and the magnitude of the anisotropy is greatest ($\mu_0^{min} = 0.1$, $\mu_0^{max} = 0.6$), the faults propagate parallel to the weakest direction of the host rock (Figures 5d–5f). In simulations with lower anisotropy ($\mu_0^{min} > 0.1$, $\mu_0^{max} = 0.6$), the faults initially propagate parallel to each other (in-line propagation), and then propagate toward each other at shallow angles, propagating just outside of the regions of highest efficiency in the isotropic model's propagation forecast envelopes (Figures 5d–5f). In the first increment of fault growth, the gain in efficiency of new faults orientated along $\theta_{min} = 180°$ is sufficient to shift the optimal propagation direction from 200° to 180° for all tested strengths (Figure 5e). However, after the first increment of growth, the faults do not propagate along the weakest direction of the host rock in systems with $\mu_0^{min} > 0.1$ (Figure 5f). After the first initial increments of fault growth, the influence of the fault tip stress field is greater than the influence of the material anisotropy. When $\theta_{min} = 200°$ and μ_0^{min} ranges from 0.1 to 0.4, the overall predicted fault geometry remains unchanged (Figures 5g–5i).

5. Predictions of Hayward Fault Propagation

To investigate the linkage of the Hayward and Rodgers Creek faults, we simulate the propagation of the Hayward Fault in two models with fault geometries that differ in the length of modeled Rodgers Creek Fault. This represents the epistemic uncertainty in the active Rodgers Creek geometry at the time that the Hayward Fault propagated. In one model, the Rodgers Creek Fault initially forms an overlapping step over

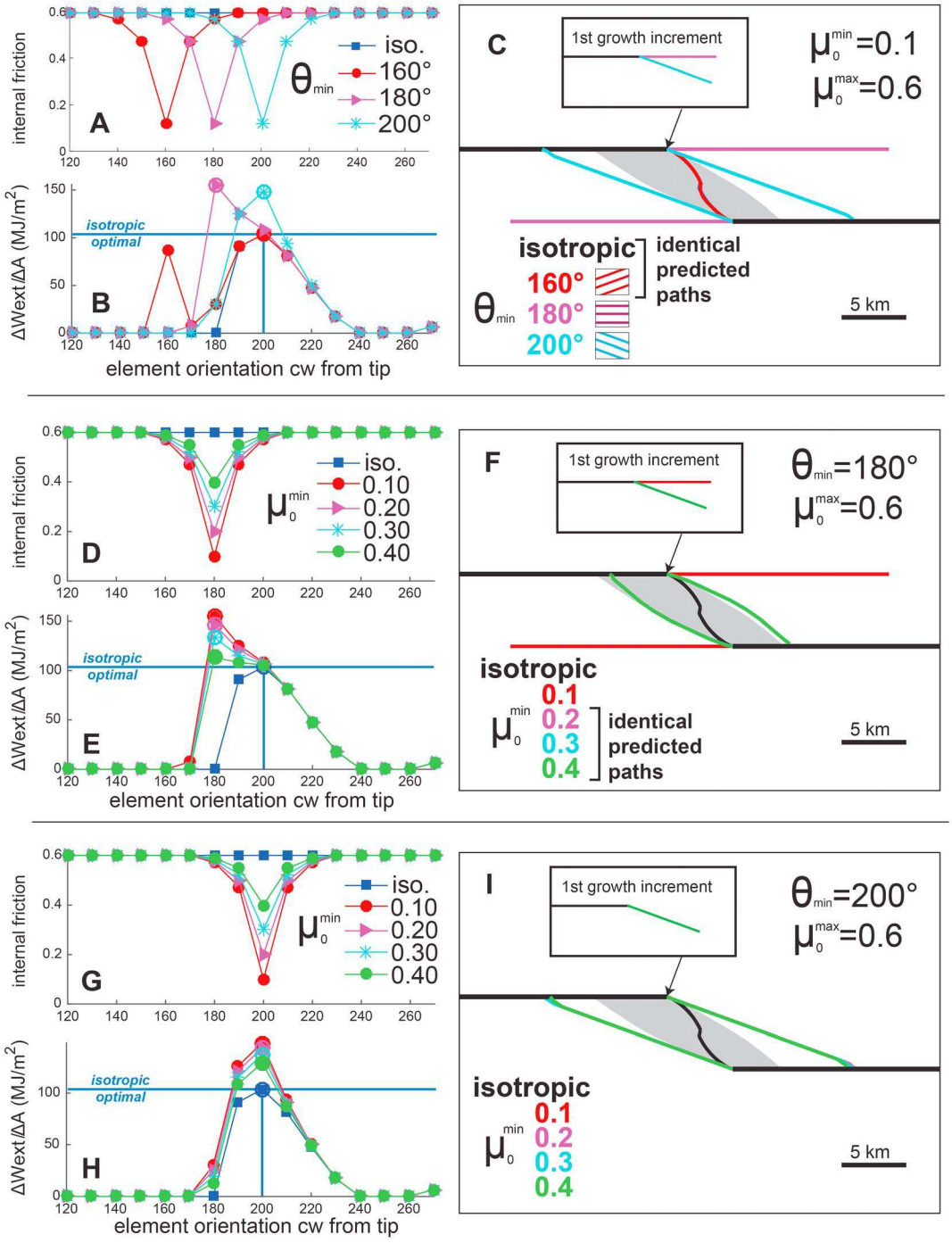

Figure 5. Predicted fault geometries for anisotropic systems. Varying anisotropy direction, θ_{min}, from 160° (red), 180° (pink), and 200° (light blue), with φ = 30°, μ_0^{max} = 0.6, and μ_0^{min} = 0.1. Distribution of μ_0 in first increment of growth at the tip of (a) upper left fault (simplified Rodgers Creek Fault), resulting (b) $\Delta W_{ext}/\Delta A$ at this growth increment, and (c) complete propagation paths for each anisotropic system. (d–f) Varying anisotropy magnitude with μ_0^{min} from 0.1 (red), 0.2 (pink), 0.3 (blue), and 0.4 (green), with θ_{min} = 180°, φ = 30°, and μ_0^{max} = 0.6. (g–i) Varying anisotropy magnitude with μ_0^{min} from 0.1 (red), 0.2 (pink), 0.3 (blue), and 0.4 (green), with θ_{min} = 200°, φ = 30°, and μ_0^{max} = 0.6. The gray shaded regions in Figures 5c, 5f, and 5i indicate extent of 90% propagation forecast envelope.

with the Hayward Fault, following the geometry inferred from early geophysical imaging that identified the extension of the Rodgers Creek Fault within the San Pablo Bay (Parsons et al., 2003). In the other model, the active Rodgers Creek Fault initially forms an underlapping step over, following the geometry inferred from recent geophysical imaging that did not find evidence of recent slip along the Rodgers Creek Fault within the San Pablo Bay (Watt et al., 2016).

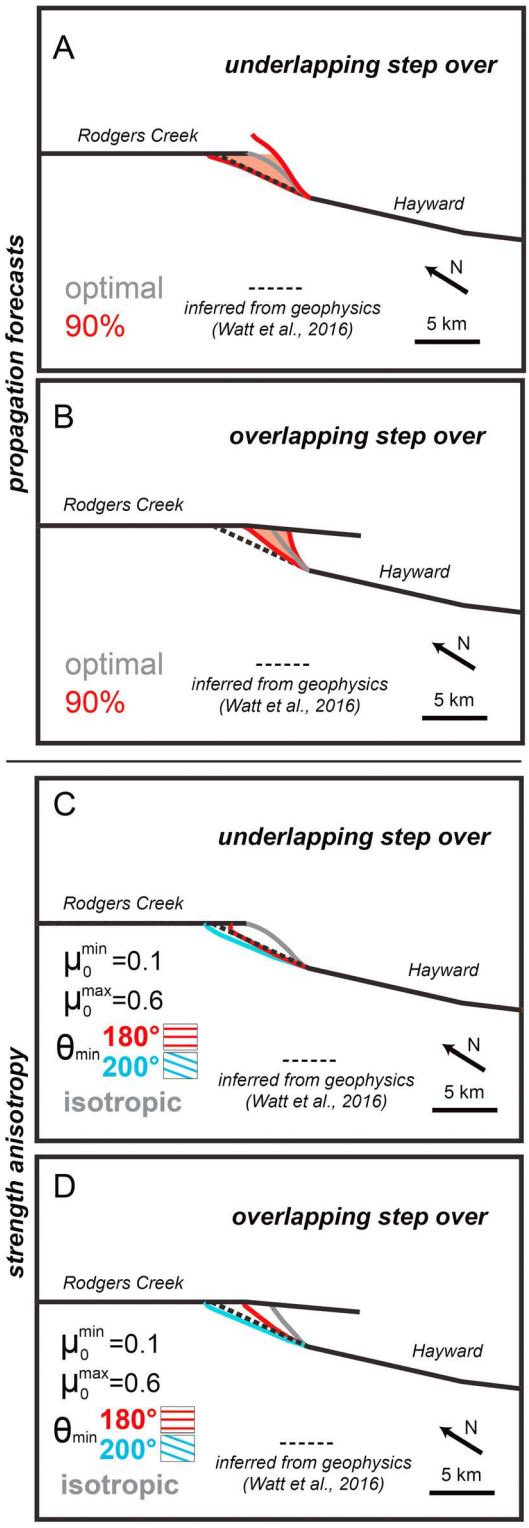

Figure 6. Optimal path (gray) and propagation forecasts (red) of Hayward Fault for (a) underlapping and (b) overlapping models. The dashed lines indicate fault geometry inferred from geophysical imaging of Watt et al. (2016). Predicted optimal Hayward propagation in anisotropic systems for (c) underlapping and (d) overlapping step over models. Isotropic predictions shown in gray and anisotropic systems with $\varphi = 30°$, $\mu_0^{min} = 0.1$, $\mu_0^{max} = 0.6$, and $\theta_{min} = 180°$ shown in red and $\theta_{min} = 200°$ shown in blue.

5.1. Propagation Forecasts of the Hayward Fault in Isotropic Host Rock

In both models with initially underlapping and overlapping steps, the Hayward Fault propagates to the north and then links with the Rogers Creek in final configurations that resemble those found by Watt et al. (2016) (Figure 6). In the underlapping step over simulation, which represents the configuration when this portion of the Rodgers Creek Fault within the San Pablo Bay is inactive, the inferred trace of the Hayward Fault lies within the 90% propagation forecast envelope (Figure 6a). In the overlapping simulation, the inferred Hayward Fault trace lies mostly outside of the 90% propagation forecast, with only the leftmost (northwest) edge of the 90% propagation forecast intersecting a <1 km portion of the inferred Hayward trace (Figure 6b). The optimal Hayward fault propagation path predicted in the underlapping step over simulation is closer to the geophysically inferred Hayward trace than the optimal path predicted in the overlapping step over simulation.

5.2. Hayward Fault Propagation in Anisotropic Rock

Similar to the models with simplified fault geometries, in these models, we vary θ_{min} from 180° to 200° to capture the range of the dominant strength anisotropy direction in the region (e.g., Wakabayashi, 1992). When the $\theta_{min} = 160°$, the resulting fault propagation paths match the propagation paths predicted in the isotropic system. In both suites of models with differing Rodgers Creek Fault geometries, when $\theta_{min} = 200°$, the predicted Hayward Fault propagation paths are within 0.5 km of the geophysically inferred fault trace along its entire length (Figure 6c). In the overlapping step over model with $\theta_{min} = 180°$, the predicted Hayward Fault path curves toward the Rodgers Creek Fault at a sharper angle than the geophysically inferred fault trace (Figure 6d). In general, propagation of the Hayward Fault in the underlapping step over model is less sensitive to the tested 20° range of θ_{min} (Figure 6c) than in the overlapping step over model (Figure 6d). In the underlapping step over model with $\theta_{min} = 180°$, the predicted path of the Hayward Fault coincides with the inferred Hayward trace along $>90\%$ of its length.

The reduced sensitivity of the Hayward Fault propagation path to θ_{min} in the underlapping step over model indicates that the local stress field near the Hayward Fault tip exerts greater influence on its growth than in the overlapping step over model. This dominance of the local stress field over material strength anisotropy is supported by the elevated mode II stress intensity factor at the propagating Hayward Fault element tip in the underlapping step over model (2,248 MPa * $m^{1/2}$) relative to the overlapping step over model (2,064 MPa * $m^{1/2}$).

Propagation of the Hayward Fault within an initially underlapping step produces the geophysically inferred fault geometry of the Hayward Fault (Watt et al., 2016) with isotropic strength. This agreement between predicted and inferred fault geometry remains consistent for a range of strength anisotropy directions in the underlapping step over model. However, in the overlapping step over model, the predicted fault propagation paths differ from the

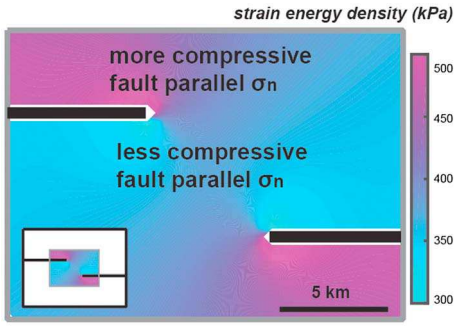

Figure 7. Strain energy density (SED) field of planar fault model with initial fault geometry.

geophysically inferred trace in isotropic host rock when the anisotropic direction is <200°.

6. Discussion

The simplified fault geometry simulations presented here shed insight on the interaction of underlapping, planar, parallel faults as they grow into an extensional step over, and the evolution of mechanical efficiency of the fault system due to fault growth and linkage, in both isotropic and anisotropic strength host rocks. We discuss the implications of the propagation paths predicted by work optimization in models with the differing fault configurations and the seismic hazard implications of the northern end of the Hayward fault linking with southern end of the Rodgers Creek fault.

6.1. Growth of Planar Underlapping Faults Within an Extensional Step in Heterogeneous and Anisotropic Rock

We find that pervasive host rock anisotropy can exert a significant influence on fault development. Both the magnitude and direction of host rock strength anisotropy can impact fault propagation, interaction, and linkage. A difference in internal friction coefficient of 33%, from 0.6 to 0.4, is sufficient to cause the predicted propagation paths to deviate from those for the isotropic system (Figure 5). A difference in the anisotropy direction of 20° can alter the predicted propagation paths when the anisotropy orientation promotes fault growth into the less compressional region of the step over between the fault segments. The range of the fault propagation forecasts considered for models with isotropic host rock represents the potential impact of small local heterogeneities on fault growth. The degree of heterogeneity considered by a particular propagation forecast (e.g., 95% of maximum ΔW_{ext}) depends the total internal work stored in the system. Here we find that the tested range of host rock strength anisotropy produces fault propagation outside the 90% of ΔW_{ext} isotropic forecast envelope (Figure 5). This result indicates that larger envelopes that arise from greater heterogeneity sensitivity would be required to capture the effects of the tested range of host rock strength anisotropy when simulating fault propagation through isotropic host rock. Consequently, using propagation forecasts that consider heterogeneity as a proxy for host rock anisotropy may not provide reliable predictions of fault propagation.

6.2. Predictions of Fault Propagation Using External Work Versus Strain Energy Density

Previous numerical approaches have predicted that faults will grow into regions with high strain energy density (SED), which are regions of stored host rock deformation (e.g., Del Castello & Cooke, 2007; Du & Aydin, 1993; Okubo & Schultz, 2005; Olson & Cooke, 2005). Fault propagation into high SED regions should produce a higher gain in efficiency than fault propagation into low SED regions because the resulting greater fault slip will reduce the work done in internal host rock deformation, that is, the internal work (Cooke and Madden, 2014), reducing the total external work. The SED field, including both the dilational and distortional components, around the initial fault tips in the planar fault simulations is lower between the fault tips than outside of the step (Figure 7) because the fault parallel normal stresses are less compressional between the tips and the local tension offsets the overall lithostatic compression. However the distribution of $\Delta W_{ext}/\Delta A$ for all potential growth elements in the first increment of growth (Figure 4b) reveals that the higher compressive stresses outside the step over prevent elements oriented at <180° from failing. The most efficient orientation in the first increment of growth is within 20° of the initial fault strike, but on the inside of the step over where SED is lesser. This preferred element orientation indicates that there is a competition between fault propagation into regions with high stresses and strains, producing high SED, and the clamping of potential fault elements by more compressional normal stresses that prevent failure and propagation into those high SED regions. Work optimization provides a more robust prediction of fault propagation than SED distribution alone.

6.3. Fault Geometry Within San Pablo Bay

The match of the modeled Hayward Fault geometry to the geophysically inferred geometry in simulations with an underlapping initial step over geometry suggests that the mapped portion of the Rodgers Creek

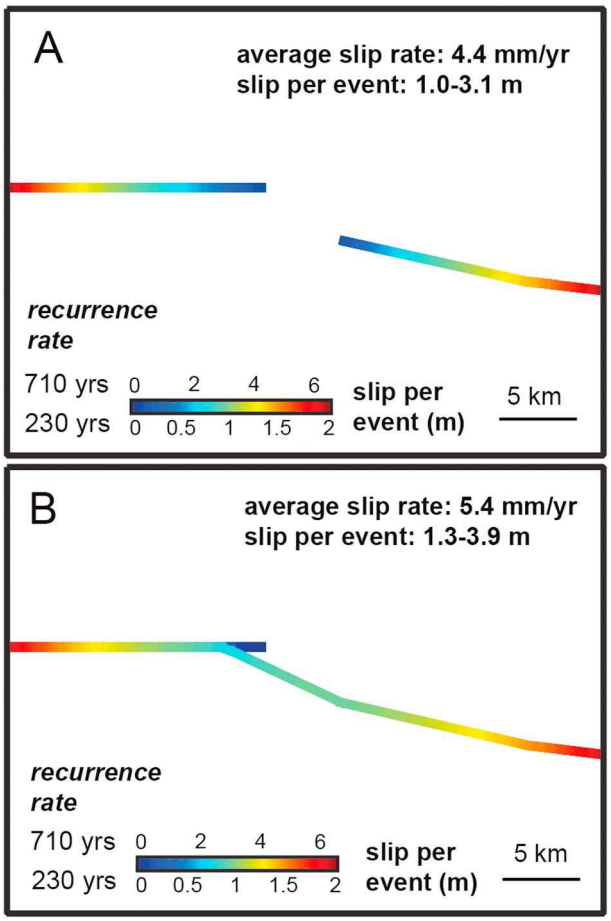

Figure 8. Average slip per event along faults. Models with (a) unconnected and (b) connected Rodgers Creek and Hayward faults with the minimum (230 years) and maximum (710 years) recurrence intervals estimated for each fault.

Fault within San Pablo Bay was inactive when the Hayward Fault propagated through the bay. Marine magnetic anomalies, gravity gradients, and seismic reflection data provide evidence of slip along the Hayward Fault within the upper 5 m of the San Pablo Bay (Watt et al., 2016), and these data do not indicate recent slip along the potential portion of the Rodgers Creek Fault that lies within the bay, which was mapped from deeper geophysical data (Parsons et al., 2003). The predicted fault geometries do not exclude the possibility that the Rodgers Creek Fault was active in this location before growth of the Hayward Fault and its linkage to the Rodger Creek Fault. The models presented here are consistent with the more recent interpretations, which suggest that the activity on the southern Rodgers Creek Fault is limited to northwest of the bay (Watt et al., 2016).

The similar fault propagation paths predicted in simulations with different anisotropy directions and the same initial fault configurations indicate that the local fault tip stress field controlled the fault propagation paths to a greater degree than the host rock anisotropy tested here (Figure 6). The difference in predicted paths between models with different initial fault configurations further reveals this control of local stress field on propagation path. The differing initial fault configurations produces differing local fault tip stress fields that promote fault growth along different trajectories.

6.4. Seismic Hazard in San Pablo Bay Area

To assess the seismic hazard implications of a hard link between the northern Hayward and southern Rodgers Creek faults at seismogenic depths, we calculate the slip per event in two models that both terminate the active Rodgers Creek Fault near the bay edge: in one model the faults are connected, and in the other, they are not connected (Figure 8). To estimate earthquake magnitude from these models, we use the average slip along the modeled faults, the recurrence interval of the faults estimated from historical and paleoseismic data, and the empirical relationship of average slip to moment magnitude of Wells and Coppersmith (1994). We estimate the modeled slip per event as the average slip rate along the two faults divided by the number of earthquakes expected to occur within the simulated time interval (2,500 years). We find the expected number of earthquakes as the simulated time interval divided by the recurrence intervals for the Rodgers Creek and Hayward faults, which are 230 and 710 years, respectively (Hayward Fault Paleoearthquake Group, 1999; Schwartz et al., 1992).

The model with the connected faults produces higher average slip rate (5.4 mm/yr) and slip per event (1.3–3.9 m) relative to the unconnected fault model (4.4 mm/yr, 1.0–3.1 m), because fault linkage facilitates slip transfer between the faults. The low slip along the portion of the Rodgers Creek Fault to the southeast of the linking segment highlights the transfer of dextral slip from one fault to the other across the linking segment (Figure 8). The reported range in slip per event reflects the range in recurrence interval estimated for the Hayward Fault and Rodgers Creek Fault. The minimum estimates of average slip per event from both models (1.3 m and 1.0 m) are similar to estimates of slip per event derived from paleoseismic data near the southern end of the Rodgers Creek Fault from offset channels in late Holocene alluvial deposits at the Beebe Ranch site (1.8–2.3 m) (Budding et al., 1991; Schwartz et al., 1992) and an offset channel at the Triangle G Ranch site (1.6–3.4 m) (Hecker et al., 2005). The largest surface rupture estimated for the Rodgers Creek Fault at the Beebe Range site (2.8–5.4 m) (Budding et al., 1991) more closely matches the maximum estimates of slip per event from both models (3.9 m and 3.1 m). The estimates of slip per event from both models are also similar to geodetically inferred slip in the 1868 Hayward Fault earthquake (1.4–2.3 m) (Yu & Segall, 1996). We cannot use the model estimates of average slip per event to discriminate between the connected and segmented fault geometries as both models agree with paleoseismic estimates.

The estimates of average dextral slip rate in both models (5.4 mm/yr and 4.4 mm/yr) are lower than geologic estimates. The latest Pleistocene to Holocene slip rate for the northern Hayward Fault section is constrained from dextral offset of a marine-abrasion-platform embayment in the Point Pinole area (site 55a-1, 3.5 mm/yr) (Borchardt, 1998). Offset channels at the Beebe Ranch site indicate that the dextral slip rate of the Rodgers Creek Fault is 6.4–10.4 mm/yr (Schwartz et al., 1992), with a minimum slip rate of 2.1–5.8 mm/yr for the past 1,300 years (Budding et al., 1991). This discrepancy between the geologic measurements and model results likely occurs because the field measurements were taken outside of the San Pablo Bay region, where fault geometry is simpler. In contrast, the model results indicate average slip rate within the San Pablo Bay, where the local fault complexity likely reduces strike-slip rates. The Triangle G and Beebe Range sites are along the Rogers Creek Fault ~15 km northwest of the edge of the San Pablo Bay and consequently lie just outside the left (northwest) edge of our model domain.

Empirical relationships of average surface slip per event to moment magnitude indicate that the range in average earthquake magnitude from estimates of both models is *M* 7.1–7.6 (Wells & Coppersmith, 1994), with the larger magnitude corresponding to the linked fault system. This range agrees with estimates from geodetically inferred slip on the Hayward Fault in the 1868 earthquake (*M* 7) (Yu & Segall, 1996) and estimates from historical earthquakes and paleoseismic slip rates due to the combined rupture of the Hayward and Rodgers Creek faults (*M* 7.09–7.39) (Schwartz et al., 2014).

Although these results do not allow us to distinguish the likelihood of a fully linked versus a segmented fault system within the step, it is clear that both can produce destructive earthquakes. Because the modeled growth of the Hayward Fault matches the geometry inferred by Watt et al. (2016), which includes linkage, we emphasize that this hard-linked fault configuration has the potential to produce earthquakes up to *M* 7.6.

7. Conclusions

To investigate the geometry of the Rodgers Creek-Hayward Fault system at seismogenic depths in the San Pablo Bay, we simulate the propagation and interaction of the northern Hayward Fault and the southern Rodgers Creek Fault. Simulations of fault evolution in extensional step overs between planar faults produce geometries similar to those observed in the early stages of extensional step over development (e.g., Mann et al., 1983). Propagation forecasts of fault development suggest that the optimal configuration of the first linking structure between two underlapping faults in an extensional step over is a single transfer fault (Figure 4). Less efficient propagation paths defined by propagation forecast envelopes form wider basins as the propagation power, or rate of efficiency gain, decreases. Depending on the orientation and magnitude of host rock strength anisotropy, either anisotropy or the local fault tip stress field controls the fault propagation path (Figure 5). For the growth of parallel faults in an initially underlapping extensional step over, the orientation of the planes of weakness must be within 20° of the initial fault strike to impact the fault propagation path. The magnitude of the weakest orientation of anisotropy must be 33% less than the maximum strength to cause the predicted fault propagation paths to deviate from those in isotropic rock.

Models with more realistic initial fault geometries support a step geometry in which the Rodgers Creek Fault does not extend far into the San Pablo Bay, as proposed by Watt et al. (2016). These models predict Hayward Fault propagation that more closely matches the inferred geometry than models with an initially overlapping step in all but one simulation (Figure 6). When the anisotropy direction is 20° from the Rodgers Creek Fault strike, both simulations with initially underlapping and overlapping steps produce Hayward Fault geometries similar to the geophysically inferred trace. In models with an initially underlapping step, a difference of 20° in the anisotropy direction only minimally changes the predicted Hayward Fault propagation path, indicating that fault propagation is relatively insensitive to changes in anisotropy direction for this step over configuration. Our model results suggest that the expected host rock strength anisotropy of this region promotes linkage between the Hayward and Rodgers Creek faults in San Pablo Bay. This linkage has the potential to produce earthquakes as large as *M* 7.6 (Figure 8).

Acknowledgments
This work was supported by NSF grant EAR-1219919 to M.C. GROW and numerical models are available on GitHub (https://github.com/mlcooke/GROW). Editor Niemi and two anonymous reviewers improved the manuscript.

References

Bailey, E. H., Irwin, W. P., & Jones, D. L. (1964). The Franciscan and related rocks and their significance in the geology of western California. *California Division of Mines and Geology Bulletin*, *183*, 177.

Bellahsen, N., & Daniel, J. M. (2005). Fault reactivation control on normal fault growth: And experimental study. *Journal of Structural Geology*, *27*(4), 769–780. https://doi.org/10.1016/j.jsg.2004.12.003

Blake, M. C., Howell, D. G., & Jayko, A. S. (1984). Tectono-stratigraphic terranes of the San Francisco Bay region. In M. C. Blake Jr. (Ed.), *Franciscan geology of northern California* (Vol. 43, pp. 5–22). Bakersfield, CA: Society of Economic Paleontologists and Mineralogists, The Pacific Section.

Bonini, M., Souriot, T., Boccaletti, M., & Brun, J. P. (1997). Successive orthogonal and oblique extension episodes in a rift zone: Laboratory experiments with application to the Ethiopian rift. *Tectonics*, *16*(2), 347–362. https://doi.org/10.1029/96TC03935

Borchardt, G. (1998). Slip rate of the northern Hayward fault at Point Pinole, California: U.S. Geological Survey National Earthquake Hazards Reduction Program, Annual Summaries, v. 39. USGS Contract No. 1434-HQ-97-GR-03103 (http://erp-web.er.usgs.gov/).

Brownlee, S. J., Schulte-Pelkum, V., Raju, A., Mahan, K., Condit, C., & Orlandini, O. F. (2017). Characteristics of deep crustal seismic anisotropy from a compilation of rock elasticity tensors and their expression in receiver functions. *Tectonics*, *36*, 1835–1857. https://doi.org/10.1002/2017TC004625

Budding, K. E., Schwartz, D. P., & Oppenheimer, D. H. (1991). Slip rate, earthquake recurrence, and seismogenic potential of the Rodgers Creek fault zone, northern California: Initial results. *Geophysical Research Letters*, *18*(3), 447–450. https://doi.org/10.1029/91GL00465

Bürgmann, R., Pollard, D. D., & Martel, S. J. (1994). Slip distributions on faults: Effects of stress gradients, inelastic deformation, heterogeneous host-rock stiffness, and fault interaction. *Journal of Structural Geology*, *16*(12), 1675–1690. https://doi.org/10.1016/0191-8141(94)90134-1

Byerlee, J. (1978). Friction of rocks. *Pure and Applied Geophysics*, *116*(4-5), 615–626. https://doi.org/10.1007/BF00876528

Chester, J. S., & Fletcher, R. C. (1997). Stress distribution and failure in anisotropic rock near a bend on a weak fault. *Journal of Geophysical Research*, *102*(B1), 693–708. https://doi.org/10.1029/96JB02791

Coleman, R. G. (2000). Prospecting for ophiolites along the California continental margin. In Y. D. Dilek et al. (Eds.), *Ophiolites and oceanic crust: New insights from field studies and the ocean drilling program*, *Geological Society of America Special Paper* (Vol. 349, pp. 351–364). Boulder, CO. https://doi.org/10.1130/0-8137-2349-3.351

Collettini, C., Niemeijer, A., Viti, C., & Marone, C. (2009). Fault zone fabric and fault weakness. *Nature*, *462*(7275), 907–910. https://doi.org/10.1038/nature08585

Cooke, M. L., & Madden, E. H. (2014). Is the Earth Lazy? A review of work minimization in fault evolution. *Journal of Structural Geology*, *66*, 334–346.

Cooke, M. L., & Pollard, D. D. (1997). Bedding plane slip in initial stages of fault-related folding. *Journal of Structural Geology*, *19*(3-4), 567–581. https://doi.org/10.1016/S0191-8141(96)00097-1

Cooke, M. L., Schottenfeld, M. T., & Buchanan, S. W. (2013). Evolution of fault efficiency at restraining bends within wet kaolin analog experiments. *Journal of Structural Geology*, *51*, 180–192. https://doi.org/10.1016/j.jsg.2013.01.010

Cooke, M. L., Reber, J. E., & Haq, S. (2016). Physical experiments of tectonic deformation and processes: Building a strong community. *GSA Today*, *26*(12), 36–37.

Cowie, P. A., Gupta, S., & Dawers, N. H. (2000). Implications of fault array evolution for synrift depocentre development: Insights from a numerical fault growth model. *Basin Research*, *12*(3-4), 241–261. https://doi.org/10.1046/j.1365-2117.2000.00126.x

Crider, J. G., & Pollard, D. D. (1998). Fault linkage: Three-dimensional mechanical interaction between echelon normal faults. *Journal of Geophysical Research*, *103*(B10), 24,373–24,391. https://doi.org/10.1029/98JB01353

Cunningham, W. D., & Mann, P. (2007). Tectonics of strike-slip restraining and releasing bends. *Geological Society, London, Special Publications*, *290*(1), 1–12.

Daly, M. C., Chorowicz, J., & Fairhead, D. (1989). Rift basin evolution in Africa: The influence of reactivated steep basement shear zones. In M. A. Cooper & G. D. Williams (Eds.), *Inversion tectonics*, *Geological Society of London Special Publication* (Vol. 44, pp. 309–334). London: Geological Society of London.

Del Castello, M., & Cooke, M. L. (2007). Underthrusting-accretion cycle: Work budget as revealed by the boundary element method. *Journal of Geophysical Research*, *112*, B12404. https://doi.org/10.1029/2007JB004997

Del Ventisette, C., Montanari, D., Sani, F., & Bonini, M. (2006). Basin inversion and fault reactivation in laboratory experiments. *Journal of Structural Geology*, *28*(11), 2067–2083. https://doi.org/10.1016/j.jsg.2006.07.012

Dixon, T. H., Stern, R. J., & Hussein, I. M. (1987). Control of Red Sea rift geometry by Precambrian structures. *Tectonics*, *6*(5), 551–571. https://doi.org/10.1029/TC006i005p00551

Dooley, T., & McClay, K. (1997). Analog modeling of pull-apart basins. *AAPG Bulletin*, *81*(11), 1804–1826.

Dooley, T. P., & Schreurs, G. (2012). Analogue modelling of intraplate strike-slip tectonics: A review and new experimental results. *Tectonophysics*, *574*, 1–71.

Dooley, T., McClay, K., & Bonora, M. (1999). January. 4D evolution of segmented strike-slip fault systems: Applications to NW Europe. In *Geological Society, London, Petroleum Geology Conference Series* (Vol. 5, pp. 215–225). Geological Society of London.

Du, Y., & Aydin, A. (1993). The maximum distortional strain energy density criterion for shear fracture propagation with applications to the growth paths of en echelon faults. *Geophysical Research Letters*, *20*(11), 1091–1094. https://doi.org/10.1029/93GL01238

Duan, K., & Kwok, C. Y. (2016). Evolution of stress-induced borehole breakout in inherently anisotropic rock: Insights from discrete element modeling. *Journal of Geophysical Research: Solid Earth*, *121*, 2361–2381. https://doi.org/10.1002/2015JB012676

Duan, K., Kwok, C. Y., & Pierce, M. (2016). Discrete element method modeling of inherently anisotropic rocks under uniaxial compression loading. *International Journal for Numerical and Analytical Methods in Geomechanics*, *40*(8), 1150–1183. https://doi.org/10.1002/nag.2476

Dubois, A., Odonne, F., Massonnat, G., Lebourg, T., & Fabre, R. (2002). Analogue modelling of fault reactivation: Tectonic inversion and oblique remobilisation of grabens. *Journal of Structural Geology*, *24*(11), 1741–1752. https://doi.org/10.1016/S0191-8141(01)00129-8

Escartin, J., Hirth, G., & Evans, B. (1997). Nondilatant brittle deformation of serpentinites: Implications for Mohr-Coulomb theory and the strength of faults. *Journal of Geophysical Research*, *102*(B2), 2897–2913. https://doi.org/10.1029/96JB02792

Faccenna, C., Nalpas, T., Brun, J. P., & Davy, P. (1995). The influence of preexisting thrust fault on normal fault geometry in nature and in experiments. *Journal of Structural Geology*, *17*(8), 1139–1149. https://doi.org/10.1016/0191-8141(95)00008-2

Ferrill, D. A., Morris, A. P., & Smart, K. J. (2007). Stratigraphic control on extensional fault propagation folding: Big Brushy Canyon monocline, Sierra del Carmen, Texas. *Geological Society, London, Special Publications*, *292*(1), 203–217. https://doi.org/10.1144/SP292.12

Field, E. H., Biasi, G. P., Bird, P., Dawson, T. E., Felzer, K. R., Jackson, D. D., … Milner, K. R. (2015). Long-term time-dependent probabilities for the third Uniform California Earthquake Rupture Forecast (UCERF3). *Bulletin of the Seismological Society of America*, *105*(2A), 511–543. https://doi.org/10.1785/0120140093

Graymer, R. W., Ponce, D. A., Jachens, R. C., Simpson, R. W., Phelps, G. A., & Wentworth, C. M. (2005). Three-dimensional geologic map of the Hayward fault, northern California: Correlation of rock units with variations in seismicity, creep rate, and fault dip. *Geology*, *33*(6), 521–524. https://doi.org/10.1130/G21435.1

Gudmundsson, A., Simmenes, T. H., Larsen, B., & Philipp, S. L. (2010). Effects of internal structure and local stresses on fracture propagation, deflection, and arrest in fault zones. *Journal of Structural Geology*, *32*(11), 1643–1655. https://doi.org/10.1016/j.jsg.2009.08.013

Harris, R. A., & Day, S. M. (1999). Dynamic 3D simulations of earthquakes on en echelon faults. *Geophysical Research Letters*, *26*(14), 2089–2092. https://doi.org/10.1029/1999GL900377

Hatem, A. E., Cooke, M. L., & Madden, E. H. (2015). Evolving efficiency of restraining bends within wet kaolin analog experiments. *Journal of Geophysical Research: Solid Earth*, *120*, 1975–1992. https://doi.org/10.1002/2014JB011735

Hayward Fault Paleoearthquake Group (1999). Timing of paleoearthquakes on the northern Hayward fault—Preliminary evidence in El Cerrito, California. *U.S. Geological Survey Open-File Report, 99–318*, pp. 34.

Hecker, S., Pantosti, D., Schwartz, D. P., Hamilton, J. C., Reidy, L. M., & Powers, T. J. (2005). The most recent large earthquake on the Rodgers Creek fault, San Francisco Bay area. *Bulletin of the Seismological Society of America*, *95*(3), 844–860. https://doi.org/10.1785/0120040134

Henza, A. A., Withjack, M. O., & Schlische, R. W. (2010). Normal-fault development during two phases of non-coaxial extension: An experimental study. *Journal of Structural Geology*, *32*(11), 1656–1667. https://doi.org/10.1016/j.jsg.2009.07.007

Holdsworth, R. E., Van Diggelen, E. W. E., Spiers, C. J., De Bresser, J. H. P., Walker, R. J., & Bowen, L. (2011). Fault rocks from the SAFOD core samples: Implications for weakening at shallow depths along the San Andreas Fault, California. *Journal of Structural Geology*, *33*(2), 132–144. https://doi.org/10.1016/j.jsg.2010.11.010

Kattenhorn, S. A., & Pollard, D. D. (2001). Integrating 3-D seismic data, field analogs, and mechanical models in the analysis of segmented normal faults in the Wytch Farm oil field, southern England, United Kingdom. *AAPG Bulletin*, *85*(7), 1183–1210.

Lettis, W., Bachhuber, J., Witter, R., Brankman, C., Randolph, C. E., Barka, A., … Kaya, A. (2002). Influence of releasing step overs on surface fault rupture and fault segmentation: Examples from the 17 August 1999 Izmit earthquake on the North Anatolian Fault, Turkey. *Bulletin of the Seismological Society of America*, *92*(1), 19–42. https://doi.org/10.1785/0120000808

Li, Q., Liu, M., & Zhang, H. (2009). A 3-D viscoelastoplastic model for simulating long-term slip on non-planar faults. *Geophysical Journal International*, *176*(1), 293–306. https://doi.org/10.1111/j.1365-246X.2008.03962.x

Lisjak, A., Taton, B. S., Grasselli, G., & Vietor, T. (2014). Numerical modeling of the anisotropic mechanical behavior of opalinus clay at the laboratory-scale using FEM/DEM. *Rock Mechanics and Rock Engineering*, *47*(1), 187–206. https://doi.org/10.1007/s00603-012-0354-7

Lockner, D. A., Morrow, C., Moore, D., & Hickman, S. (2011). Low strength of deep San Andreas fault gouge from SAFOD core. *Nature*, *472*(7341), 82–85. https://doi.org/10.1038/nature09927

Madden, E., Cooke, M., & McBeck, J. (2017). Energy budget and propagation of faults via shearing and opening using work optimization. *Journal of Geophysical Research: Solid Earth*, *122*, 6757–6772. https://doi.org/10.1002/2017JB014237

Mann, P., Hempton, M. R., Bradley, D. C., & Burke, K. (1983). Development of pull-apart basins. *The Journal of Geology*, *(91)5*, 529–554.

McBeck, J., Madden, E., & Cooke, M. L. (2016). Growth by Optimization of Work (GROW): A new modeling tool that predicts fault growth through work minimization. *Computers and Geosciences*, *88*, 142–151. https://doi.org/10.1016/j.cageo.2015.12.019

McClay, K., & Dooley, T. (1995). Analogue models of pull-apart basins. *Geology*, *23*(8), 711–714. https://doi.org/10.1130/0091-7613(1995)023%3C0711:AMOPAB%3E2.3.CO;2

McConnell, R. B. (1972). Geological development of the rift system of eastern Africa. *Geological Society of America Bulletin*, *83*(9), 2549–2572. https://doi.org/10.1130/0016-7606(1972)83%5B2549:GDOTRS%5D2.0.CO;2

McLaughlin, R. J., Sarna-Wojcicki, A. M., Wagner, D. L., Flack, R. J., Langenheim, V. E., Jachens, R. C., … Allen, J. R. (2012). Evolution of the Rodgers Creek-Maacama right-lateral fault system and associated basins east of the northward-migrating Mendocino Triple Junction, northern California. *Geosphere*, *8*(2), 342–373. https://doi.org/10.1130/GES00682

Misra, S., Ellis, S., & Mandal, N. (2015). Fault damage zones in mechanically layered rocks: The effects of planar anisotropy. *Journal of Geophysical Research: Solid Earth*, *120*, 5432–5452. https://doi.org/10.1002/2014JB011780

Moore, D. E., & Lockner, D. A. (2004). Crystallographic controls on the frictional behavior of dry and water-saturated sheet structure minerals. *Journal of Geophysical Research*, *109*, B03401. https://doi.org/10.1029/2003JB002582

Morley, C. K. (2007). Variations in late Cenozoic-recent strike-slip and oblique-extensional geometries, within Indochina: The influence of pre-existing fabrics. *Journal of Structural Geology*, *29*(1), 36–58. https://doi.org/10.1016/j.jsg.2006.07.003

Morley, C. K., Haranya, C., Phoosongsee, W., Pongwapee, S., Kornsawan, A., & Wonganan, N. (2004). Activation of rift oblique and rift parallel pre-existing fabrics during extension and their effect on deformation style: Examples from the rifts of Thailand. *Journal of Structural Geology*, *26*(10), 1803–1829. https://doi.org/10.1016/j.jsg.2004.02.014

Morrow, C. A., & Lockner, D. A. (2001). Hayward fault rocks: Porosity, density and strength measurements. U.S. Department of the Interior, U.S. Geological Survey.

Okubo, C. H., & Schultz, R. A. (2005). Evolution of damage zone geometry and intensity in porous sandstone: Insight gained from strain energy density. *Journal of the Geological Society*, *162*(6), 939–949. https://doi.org/10.1144/0016-764904-148

Olson, E., & Cooke, M. L. (2005). Application of three fault growth criteria to the Puente Hills thrust system, Los Angeles, California, USA. *Journal of Structural Geology*, *27*(10), 1765–1777. https://doi.org/10.1016/j.jsg.2005.02.005

Parsons, T., Sliter, R., Geist, E. L., Jachens, R. C., Jaffe, B. E., Foxgrover, A., … McCarthy, J. (2003). Structure and mechanics of the Hayward-Rodgers Creek Fault step over, San Francisco bay, California. *Bulletin of the Seismological Society of America*, *93*(5), 2187–2200. https://doi.org/10.1785/0120020228

Peacock, D. C. P., & Sanderson, D. J. (1992). Effects of layering and anisotropy on fault geometry. *Journal of the Geological Society*, *149*(5), 793–802. https://doi.org/10.1144/gsjgs.149.5.0793

Pollitz, F. F., & Nyst, M. (2005). A physical model for strain accumulation in the San Francisco Bay region. *Geophysical Journal International*, *160*(1), 302–317.

Rahe, B., Ferrill, D. A., & Morris, A. P. (1998). Physical analog modeling of pull-apart basin evolution. *Tectonophysics*, *285*(1-2), 21–40. https://doi.org/10.1016/S0040-1951(97)00193-5

Sassi, W., Colletta, B., Bale, P., & Pacquereau, T. (1993). Modelling of structural complexity in sedimentary basins: The role of pre-existing faults in thrust tectonics. *Tectonophysics*, *226*(1-4), 97–112. https://doi.org/10.1016/0040-1951(93)90113-X

Schwartz, D. P., Pantosti, D., Hecker, S., Okumura, K., Budding, K. E., & Powers, T. (1992). Late Holocene behavior and seismogenic potential of the Rodgers Creek fault zone, Sonoma County, California. In G. Borchardt et al. (Eds.), *Proceedings of the Second Conference on Earthquake Hazards in the Eastern San Francisco Bay Area, California Division of Mines and Geology Special Publication*, *113*, (pp. 393–398).

Schwartz, D. P., Lienkaemper, J. J., Hecker, S., Kelson, K. I., Fumal, T. E., Baldwin, J. N., … Niemi, T. M. (2014). The earthquake cycle in the San Francisco Bay region: AD 1600–2012. *Bulletin of the Seismological Society of America*, *104*(3), 1299–1328. https://doi.org/10.1785/0120120322

Smith, M., & Mosley, P. (1993). Crustal heterogeneity and basement influence on the development of the Kenya Rift, East Africa. *Tectonics*, *12*(2), 591–606. https://doi.org/10.1029/92TC01710

Tong, H., & Yin, A. (2011). Reactivation tendency analysis: A theory for predicting the temporal evolution of preexisting weakness under uniform stress state. *Tectonophysics*, *503*(3–4), 195–200. https://doi.org/10.1016/j.tecto.2011.02.012

Wakabayashi, J. (1992). Nappes, tectonics of oblique plate convergence, and metamorphic evolution related to 140 million years of continuous subduction, Franciscan complex, California. *The Journal of Geology*, *100*(1), 19–40. https://doi.org/10.1086/629569

Wakabayashi, J. (2004). Contrasting settings of serpentinite bodies, San Francisco Bay area, California: Derivation from the subducting plate vs. mantle hanging wall. *International Geology Review*, *46*(12), 1103–1118. https://doi.org/10.2747/0020-6814.46.12.1103

Wakabayashi, J. (2012). Subducted sedimentary serpentinite mélanges: Record of multiple burial-exhumation cycles and subduction erosion. *Tectonophysics*, *568-569*, 230–247. https://doi.org/10.1016/j.tecto.2011.11.006

Waldhauser, F., & Schaff, D. P. (2008). Large-scale relocation of two decades of Northern California seismicity using cross-correlation and double-difference methods. *Journal of Geophysical Research: Solid Earth*, *113*, B08311. https://doi.org/10.1029/2007JB005479

Watt, J., Ponce, D., Parsons, T., & Hart, P. (2016). Missing link between the Hayward and Rodgers Creek faults. *Science Advances*, *2*(10), e1601441.

Wells, D. L., & Coppersmith, K. J. (1994). New empirical relationships among magnitude, rupture length, rupture width, rupture area, and surface displacement. *Bulletin of the Seismological Society of America*, *84*(4), 974–1002.

Wesnousky, S. G. (2008). Displacement and geometrical characteristics of earthquake surface ruptures: Issues and implications for seismic-hazard analysis and the process of earthquake rupture. *Bulletin of the Seismological Society of America*, *98*(4), 1609–1632.

Willemse, E. J. M. (1997). Segmented normal faults: Correspondence between three-dimensional mechanical models and field data. *Journal of Geophysical Research*, *102*(B1), 675–692. https://doi.org/10.1029/96JB01651

Yu, E., & Segall, P. (1996). Slip in the 1868 Hayward earthquake from the analysis of historical triangulation data. *Journal of Geophysical Research*, *101*(B7), 16,101–16,118.

Zampieri, D., Massironi, M., Sedea, R., & Sparacino, V. (2003). Strike-slip contractional stepovers in the Southern Alps (northeastern Italy). *Eclogae Geologicae Helvetiae*, *96*(1), 115–124.